Plasmonic waveguides from Coulomb-engineered two-dimensional metals

2D Materials

PAPER

Plasmonic waveguides from Coulomb-engineered two-dimensional metals

Zhihao Jiang[1], Stephan Haas[1] and Malte Rösner[2,*]

[1] Department of Physics and Astronomy, University of Southern California, Los Angeles, CA 90089-0484, United States of America
[2] Institute for Molecules and Materials, Radboud University, Heyendaalseweg 135, 6525 AJ Nijmegen, The Netherlands
* Author to whom any correspondence should be addressed.

E-mail: M.Roesner@science.ru.nl

Keywords: two-dimensional metals, plasmonic waveguides, Coulomb engineering, non-local screening, plasmon engineering, many-body properties

OPEN ACCESS

RECEIVED
21 March 2021

REVISED
20 April 2021

ACCEPTED FOR PUBLICATION
7 May 2021

PUBLISHED
25 May 2021

Abstract

Coulomb interactions play an essential role in atomically-thin materials. On one hand, they are strong and long-ranged in layered systems due to the lack of environmental screening. On the other hand, they can be efficiently tuned by means of surrounding dielectric materials. Thus all physical properties which decisively depend on the exact structure of the electronic interactions can be in principle efficiently controlled and manipulated from the outside via Coulomb engineering. Here, we show how this concept can be used to create novel plasmonic waveguides in metallic layered materials. We discuss how dielectrically structured environments can be utilized to non-invasively confine plasmonic excitations in an unperturbed homogeneous metallic two-dimensional system by modifications of its many-body interactions. We define optimal energy ranges for this mechanism and demonstrate plasmonic confinement within several nanometers. In contrast to conventional functionalization mechanisms, this scheme relies on a purely many-body concept and does not involve any direct modifications to the active material itself.

1. Introduction

Plasmons are collective excitations rendered by dynamical screened Coulomb interactions. They are hence intimately connected to a plethora of fundamental many-body material properties of electronic systems, such as their quasi-particle spectral function [1–4], optical absorption spectra [3, 5], light–matter interactions [6, 7], and possibly also to instabilities such as superconductivity [8, 9], charge-density order [10], or excitonic condensation [11]. From a technological point of view, plasmonic structures such as antennas and waveguides have become increasingly important tools to create efficient light harvesting and guiding devices [6, 12–19]. In this context, layered materials are of particular interest due to their enhanced low-energy plasmonic response. In contrast to three-dimensional bulk materials, two-dimensionally (2D) confined plasmons have a gapless excitation spectrum with a square-root dispersion at small momenta [20–23]. As will be discussed in detail below, this yields extended excitation energy ranges in which low losses are expected [24, 25], and which can be precisely controlled from the outside by Coulomb engineering, thus rendering 2D plasmonics an exciting and technologically important field.

So far, 2D plasmonic devices have been manufactured either by strongly invasive processes, such as structuring the activate material itself [26–30], by changes to the single-particle properties of the plasmon-hosting system [31–34], or by creating metallic heterostructures [35]. Here, we propose a truly non-invasive concept based on the external control of the Coulomb interactions within the active material. Specifically, we show how 2D plasmons in an homogeneous layered material can be spatially controlled with the help of structured dielectric environments, as depicted in figure 1. An analogous Coulomb engineering concept has been previously applied to atomically thin semiconductors [36–42] as well as to homogeneously embedded Mott insulators [43]. Here, we apply this concept to active metallic systems where possibly strong internal and external screening channels compete. Specifically, we will consider homogeneous as well as horizontally staggered dielectric environments. To this end, we

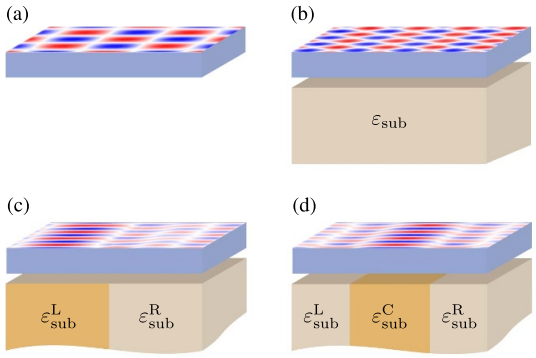

Figure 1. Substrate controlled plasmon patterns in atomically thin metals. (a) Unsupported and (b)–(d) dielectrically supported metallic layer with a typical plasmonic charge distribution. (c), (d) Structured dielectric substrates induce spatially patterned plasmonic excitations.

need to realistically account for horizontal and vertical dielectric-interface effects, which we achieve here with the help of extended image charge models valid for all length scales in combination within a real-space Random Phase Approximation (RPA) approach. Based on this, we show that plasmons can be precisely confined at certain optimal excitation energies, if the internal metallic screening is not too strong. This allows for the non-invasive creation of plasmonic waveguides, as illustrated in figure 1(d), whereby the active, plasmon hosting, monolayer remains unchanged.

2. Results and discussion

2.1. Substrate controlled 2D plasmons

In the following, we describe the plasmonic excitations in layered metals using a single-orbital generalized Hubbard model of the form

$$\hat{H} = -t \sum_{\sigma,<ij>} \hat{c}^{\dagger}_{i\sigma}\hat{c}_{j\sigma} + \sum_{i} U_{ii} n_{i\uparrow} n_{i\downarrow} + \sum_{\sigma,\sigma',i>j} U_{ij} n_{i\sigma} n_{j\sigma'}, \qquad (1)$$

where $\hat{c}^{\dagger}_{i\sigma}$ ($\hat{c}_{i\sigma}$) creates (annihilates) an electron of spin σ at the square-lattice site i, $n_{i\sigma}$ are the corresponding occupation operators, $t = 1$ eV is the nearest neighbor hopping, and U_{ij} is the non-local Coulomb interaction. We fix the lattice constant to $a_0 = 3$Å, set the Fermi energy to $E_F = -3$ eV, and treat the model within the RPA. To realistically describe the collective excitations of a generic layered metal in terms of this model we need to account for all possible screening channels. This includes intra- and inter-band polarizations within the layered material itself [20–22], as well as external polarization effects from the environment, such as substrates or capping layers. To this end, we consider the fully screened Coulomb interaction in the metallic film for in-plane momentum transfer q,

$$W(q,\omega) = \frac{v_q}{1 - v_q \Pi(q,\omega)} = \frac{v_q}{\varepsilon(q,\omega)}, \qquad (2)$$

where $\Pi(q,\omega)$, $\varepsilon(q,\omega)$, and $v_q = \frac{2\pi e^2}{q}$ are the total polarization, the dielectric function, and the bare Coulomb interaction, respectively. By splitting $\Pi = \Pi^{\rm M} + \Pi^{\rm Res}$ into the metallic polarization, resulting from intra-band transitions within the active layered material itself described by the Hamiltonian above, and a residual polarization, accounting for inter-band transitions and substrate screening, we can rewrite the fully screened Coulomb interaction as

$$W(q,\omega) = \frac{U_q}{1 - U_q \Pi^{\rm M}(q,\omega)} = \frac{U_q}{\varepsilon^{\rm M}(q,\omega)}, \qquad (3)$$

where $U_q = \frac{v(q)}{\varepsilon^{\rm Res}(q)}$ is the Fourier transform of U_{ij} accounting for the residual screening channels. The full dielectric function is thus given by the product $\varepsilon(q,\omega) = \varepsilon^{\rm M}(q,\omega)\varepsilon^{\rm Res}(q)$. We calculate $\varepsilon^{\rm M}(q,\omega)$ within the RPA based on the Hamilton from above and by neglecting local-field effects, while the residual screening can be analytically approximated from classical electrostatics, which reads for a layered material of effective height h and intrinsic dielectric constant $\varepsilon_{\rm mat}$ [21, 36, 44, 45]

$$\varepsilon^{\rm Res}(q) = \varepsilon_{\rm mat} \frac{1 - \tilde{\varepsilon}^2 e^{-2qh}}{1 + 2\tilde{\varepsilon} e^{-qh} + \tilde{\varepsilon}^2 e^{-2qh}}. \qquad (4)$$

For a dielectric encapsulation, as shown in figure 2(b), we find $\tilde{\varepsilon} = (\varepsilon_{\rm mat} - \varepsilon_{\rm sub})/(\varepsilon_{\rm mat} + \varepsilon_{\rm sub})$. This allows us to define the electron energy loss spectrum (EELS),

$$\mathrm{EELS}(q,\omega) \propto -\,\mathrm{Im}\left[\frac{1}{\varepsilon(q,\omega)}\right]. \qquad (5)$$

According to the implicit definition of plasmonic excitations, $\varepsilon(q,\omega_p(q)) = 0$, the EELS is maximized along the plasmonic dispersion $\omega_p(q)$. This way, we can extract $\omega_p(q)$ along a path in momentum space, as shown in figure 2(d) along with the metallic polarization function $\Pi^{\rm M}(q,\omega)$. The model parameters are chosen to approximately reproduce the plasmonic energy scales of metallic transition metal dichalcogenides [21, 22, 44] or doped hexagonal boron nitride [46]. We observe that even in the free-standing case ($\varepsilon_{\rm sub} = 1$) the plasmonic dispersion deviates quickly from the generic $\sqrt{q}$-like dispersion [20–22], known from purely two-dimensional models. This deviation is a consequence of the non-local residual screening $\varepsilon^{\rm Res}(q)$ induced by inter-band transitions within the layered metal, which we plot in figure 2(a). For the free-standing case, its long and short wavelength limits are $\varepsilon^{\rm Res}(q=0) = 1$ and $\varepsilon^{\rm Res}(q \gg 1) = \varepsilon_{\rm mat}$, respectively. Hence, in the long wavelength limit the effective background screening is negligible [47], and $\omega_p(q) \propto \sqrt{q}$ holds. For larger momenta, however, $\varepsilon^{\rm Res}$

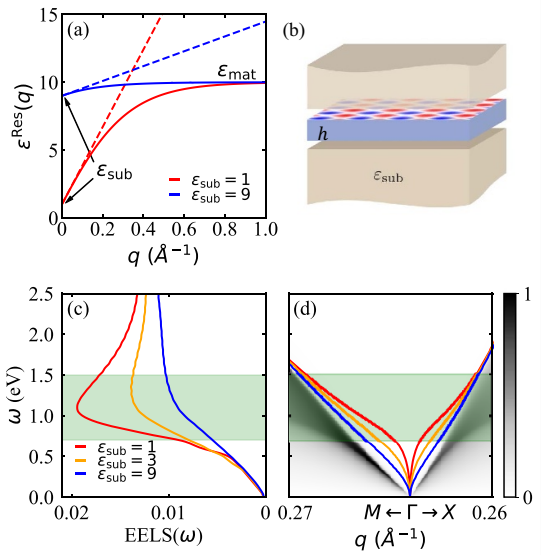

Figure 2. Substrate controlled two-dimensional plasmons. (a) Effective residual screening function $\varepsilon^{\mathrm{Res}}(q)$ for different homogeneous dielectric substrates. The dashed lines indicate the slopes of the function at $q = 0$. (b) Illustration of plasmon excitation in a layered material embedded in a homogeneous dielectric environment. (c) Electron energy loss spectra of the two-dimensional metallic monolayer shown in (b), with different choices of the environmental dielectric constant. (d) Plasmon dispersions in momentum space around Γ. The grey area represents the electron–hole continuum.

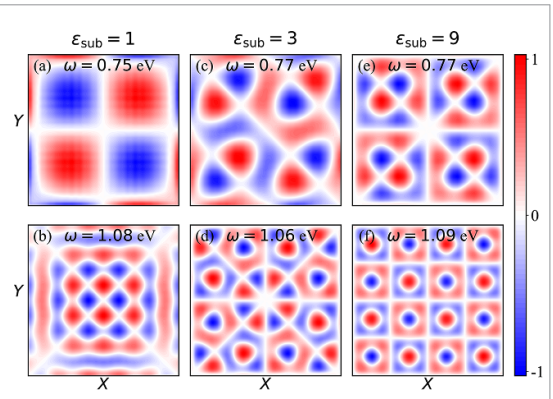

Figure 3. Real-space charge density modulations of two typical plasmon modes. At $\omega \approx 0.77$ eV and $\omega \approx 1.08$ eV, plotted for three different dielectric environments.

increases successively, which suppresses $\omega_p(q)$ and eventually pushes it into the particle-hole continuum. Importantly, the corresponding flattening of the plasmonic dispersion takes place at momenta which are clearly detached from the particle-hole continuum, so that Landau damping and thus plasmonic losses are drastically reduced in layered metals at small and intermediate momenta [20–22, 46]. This, in turn, leads to a prominent enhancement of the plasmonic spectral function at intermediate frequencies, as it is clearly visible in the EELS(ω), shown in figure 2(c) (green shaded region).

This behavior of the plasmonic dispersion relation is a generic feature of spatially confined charge densities and can thus be observed in a variety of different metallic, semimetallic, and doped semiconducting monolayer materials including graphene [23, 44, 47, 48], Li-intercalated hexagonal boron nitride [46], doped black phosphorus [49, 50], metallic T- [51, 52] and 2H-phase [20, 22] transition metal dichalcogenides, as well as in their doped 2H-phase semiconducting counterparts [21]. The details of the dispersion flattening and the corresponding energy of the enhanced spectral weight in the full EELS of these materials are highly material specific and vary between a few 100 meV to about 1–2 eV but share the common origin explained above.

Upon increasing the environmental screening, e.g. by using different substrate materials (illustrated in figure 2(b)), the long wavelength limit of the effective residual screening is changed to $\varepsilon^{\mathrm{Res}}(q = 0) = \varepsilon_{\mathrm{sub}}$. This leads to a decreased U_q and subsequently to a reduced plasmonic dispersion with enhanced slopes for small momenta. In the full EELS(ω) we correspondingly find a decreased and broadened maximum at intermediate frequencies, whereas the remainder of the plasmonic spectrum is largely unaffected. This intermediate frequency range in the plasmonic spectral function is thus most susceptible to changes in the environmental screening of the layered material.

The enhanced environmental screening sensitivity of plasmons in layered materials at intermediate excitation energies is also reflected in the corresponding real-space charge density patterns, shown in figures 3(a)–(f) at $\omega \approx 0.77$ eV and $\omega \approx 1.08$ eV for the same $\varepsilon_{\mathrm{sub}}$ as before. Here, we observe extended modes with checkerboard-like patterns oscillating along the x and y directions. At a fixed excitation energy, these patterns show decreasing wavelengths upon increasing the environmental screening, in line with the corresponding dispersions shown in figure 2(d). Similarly, we observe that the plasmonic wavelengths decrease with increasing excitation energies at fixed screening.

This demonstrates how spatial patterns of 2D plasmons can be controlled by means of dielectric substrates. In the following, we illustrate how this can be utilized to spatially confine plasmonic excitations by using structured dielectric environments.

2.2. 2D plasmons in heterogeneous screening environments

Let us now consider a heterogeneous dielectric environment with a vertical interface separating areas with $\varepsilon^{\mathrm{L}}_{\mathrm{sub}} = 1$ and $\varepsilon^{\mathrm{R}}_{\mathrm{sub}} = 9$, as depicted in figure 4(a). Since this breaks the translational symmetry along the x-direction, we are forced to switch to a real-space representation. To this end, we utilize a supercell consisting of 80 × 80 unit cells (240 Å × 240 Å) and describe the background-screened Coulomb interaction with an extended image-charge model

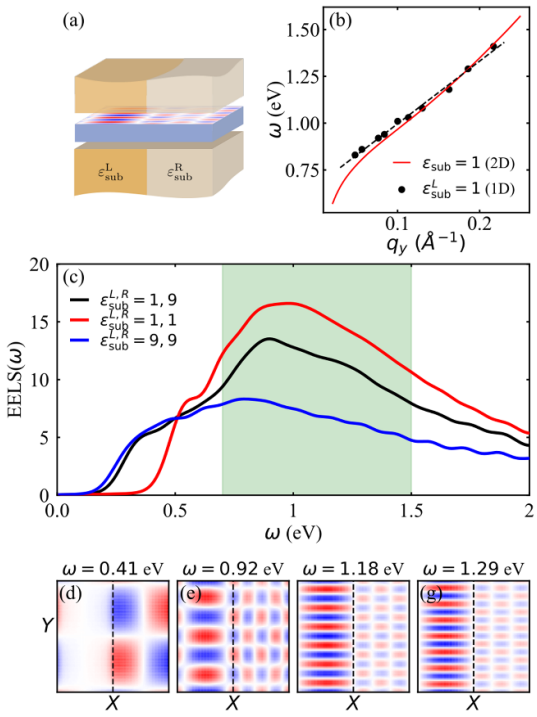

Figure 4. Heterogeneous plasmon patterns from spatially structured dielectric environments. (a) Sketch of the layered metal embedded in a heterogeneous dielectric environment. (b) Dispersion relation of the plasmon mode in the left subspace with $\varepsilon^L_{sub} = 1.0$ and $\varepsilon^R_{sub} = 9$ (black dots) together with the dispersion from figure 2(c) for $\varepsilon_{sub} = 1$. (c) Total EELS (black) for $\varepsilon^L_{sub} = 1$ and $\varepsilon^R_{sub} = 9$ together with homogeneous EELS (red and blue). (d)–(g) Typical plasmon modes at different frequencies. This figure should be just a single column wide.

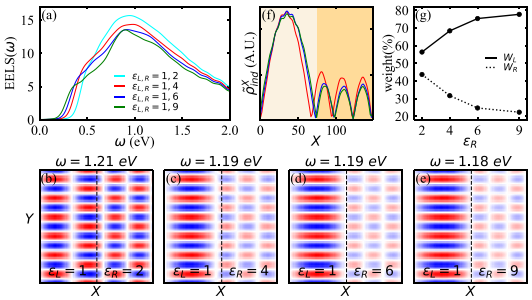

Figure 5. Impact of the dielectric contrast to the plasmonic patterns. (a) Total EELS for a different dielectric contrasts. (b)–(e) Corresponding real-space patterns for $\omega \approx 1.2$ eV. (f) Normalized x-component of the charge distributions of these plasmon modes. (g) Variation of the charge weight in the left (W_L) and right (W_R) subspaces.

(see appendix for details). In figure 4(c) we show the resulting heterogeneous EELS(ω) (black) as well as the corresponding EELS(ω) for the two homogeneous situations (red and blue). By comparing the heterogeneous spectrum to the unsupported one (i.e. $\varepsilon^L_{sub} = \varepsilon^R_{sub} = 1$), we observe that the maximum at intermediate excitation energies (green shaded) is still present, but suppressed. For excitation energies below 0.5 eV we see that the homogeneous EELS in the unsupported situation vanishes. This is a finite-size effect of the supercell calculation which suppresses all plasmons with wave-lengths larger than the supercell size, cf figure 2, which can also be seen for the supported case. The heterogeneous spectral function thus clearly inherits characteristics from both homogeneous limits. The origin of this becomes obvious by examining the corresponding real-space charge modulations. At small excitation energies, the plasmons are mostly localized in the ε^R_{sub} region, as seen in figure 4(d), whereas at intermediate excitation energies they prominently reside in the ε^L_{sub} area, as observed in figures 4(e)–(g).

This illustrates how heterogeneous plasmonic patterns can be externally and non-invasively induced in homogeneous layered materials via spatially structured substrates. The substrate induced heterogeneous plasmonic patterns behave, however, slightly differently compared to their homogeneous counterparts depicted in figure 3. For intermediate excitation energies, which mostly confine the plasmon in the ε^L_{sub} region, the resulting pattern is now quasi-one-dimensional. Specifically, we observe that its propagation direction aligns with the dielectric interface in the substrate and has a linear dispersion, as shown in figure 4(b). Additionally, there are some spurious, strongly damped, plasmonic excitations present in the ε^R_{sub} region.

Interestingly, the fully heterogeneous EELS (black line in figure 4(c)) can be approximately reconstructed by taking a simple average over the homogeneous data (blue and red lines). From this we understand that the $\varepsilon^L_{sub} = 1$ environment barely affects the low-energy plasmonic excitations confined in the $\varepsilon^R_{sub} = 9$ area, which does not hold vice versa. I.e. the $\varepsilon^R_{sub} = 9$ slightly damps the plasmonic excitations on the $\varepsilon^L_{sub} = 1$ side. However, except from this, these two patterns behave largely independently on the other side.

We proceed with a quantitative analysis of these confined excitations by investigating their dependence on the dielectric contrast $\varepsilon^R_{sub}/\varepsilon^L_{sub}$ in the substrate. To this end, we fix $\varepsilon^L_{sub} = 1$ and vary ε^R_{sub}. In figure 5(a) we observe that increasing the contrast affects the EELS in a non-trivial way. At small dielectric contrasts, the full heterogeneous EELS resembles a homogeneous one, with just one broad maximum at intermediate excitation energies, which is reflected in the rather spread-out plasmonic excitation pattern depicted in figure 5(b). Upon increasing the substrate dielectric contrast, we find an increasing localization of the plasmonic pattern on the ε^L_{sub} side, with decreasing weight on the ε^R_{sub} side for $\omega \approx 1.2$ eV, as depicted in figures 5(c)–(e). We can furthermore quantify this increasing localization with the help of the normalized charge distribution function, $\tilde{\rho}_{ind}(x)$, obtained by integrating the absolute value of the real-space charge distribution function along the y-component (see figure 5(f)).

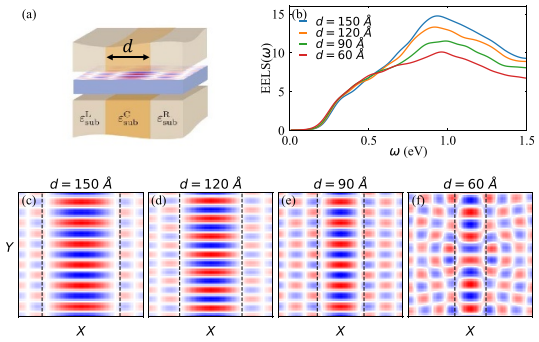

Figure 6. Plasmonic waveguides from spatially structured dielectric environments. (a) Illustration of the plasmonic waveguide design. (b) Dependence of the EELS on the core width d. (c)–(f) Real space charge modulations of typical plasmon modes at $\omega \approx 1.0$ eV.

By additionally integrating $\tilde{\rho}_{\mathrm{ind}}(x)$ over the left and right regions we can define sub-space weights $W_{\mathrm{L/R}}$, which we show in figure 5(g). We observe that up to nearly 80% of the charge can be confined within the left region for the maximum dielectric contrast considered here. As a result, the plasmonic excitation in the $\varepsilon^{\mathrm{L}}_{\mathrm{sub}}$ area gets relatively brighter. However, increasing $\varepsilon^{\mathrm{R}}_{\mathrm{sub}}$ also damps the excitation in the $\varepsilon^{\mathrm{L}}_{\mathrm{sub}}$ region. Therefore, achieving an optimal dielectric contrast will be a trade-off between spatial contrast and brightness of the plasmons on the active side. We note that the $\varepsilon^{\mathrm{L}}_{\mathrm{sub}}$-confined quasi-one-dimensional plasmon wavelength is not affected by $\varepsilon^{\mathrm{R}}_{\mathrm{sub}}$. For heterogeneous dielectric substrates only, i.e. without the structured capping layer, the very same behavior is expected but a larger dielectric contrast in the substrate will be needed to achieve the same separation.

2.3. Novel plasmonic waveguides

The possibility to non-invasively induce spatially patterned plasmonic excitations in a homogeneous layered material by means of dielectric interfaces in the dielectric environment motivates us to propose a new class of plasmonic waveguides that utilizes two parallel vertical dielectric interfaces in the environment, as illustrated in figure 6(a). This will confine well-defined quasi-one-dimensional plasmons in the central region if the substrate's dielectric constant there is smaller than in the outer substrate regions. To verify this proposal, we study below a system with $\varepsilon^{\mathrm{L}}_{\mathrm{sub}} = \varepsilon^{\mathrm{R}}_{\mathrm{sub}} = 9$ and $\varepsilon^{\mathrm{C}}_{\mathrm{sub}} = 1$, and with variable central substrate width d.

In figure 6(a) we show the EELS for various d. Starting from large d, we recover the previously discussed maximum at intermediate excitation energies. Upon decreasing d, this maximum diminishes until it vanishes below $d \lesssim 60$ Å (20 unit cells). This behavior becomes clear by examining the corresponding real-space patterns shown in figures 6(c)–(f). Figure 6(c) reveals that the plasmon mode is now indeed spatially confined in the central substrate area and propagates parallel to the substrate dielectric interfaces. Thus, the maximum in EELS(ω) results from the low-dielectric substrate region, and the correspondingly confined plasmonic excitation there. Upon decreasing d, we observe in figures 6(d)–(f) that the novel plasmonic waveguide behavior persists, but with gradually decreasing contrast to the $\varepsilon^{\mathrm{L/R}}_{\mathrm{sub}}$ areas, until it nearly vanishes for the smallest d shown in figure 6(f). Thus, the increasing environmental screening from the increasing $\varepsilon^{\mathrm{L/R}}_{\mathrm{sub}}$ regions gradually damps the confined excitation in the center of the device until no spatial structure is visible anymore. Nevertheless, a clear confinement can be achieved for waveguides with widths down to about 30 unit cells, which is on the order of 90Å here. Like in the case of the dielectric contrast, there is a trade-off between the field confinement and loss in the optimization of these plasmonic waveguides [19, 53]. This is a demonstration of a novel type of plasmonic waveguides, based on Coulomb-engineered homogeneous layered metallic materials.

3. Outlook and conclusions

3.1. Active material candidates

Apart from the properties of the structured dielectric environment, our proposal also depends strongly on the active material itself, i.e. not all 2D metals will be equally suitable. Specifically, the Coulomb interaction between the electrons in the active metallic layer should be very sensitive to environmental screening. This is the case if all layer-internal polarization channels (intra- and inter-band) are rather small, in other words: materials with a small density of states at the Fermi level (or with a small effective mass) and with a metallic (low-energy plasmon hosting) band which is energetically well separated from all other valence and conduction bands. Both of these properties are satisfied in graphene: it hosts low-loss plasmons [28, 48, 54–56], and the Coulomb interactions have been experimentally shown to be rather susceptible to external polarization [35, 47, 57]. Alternatively, slightly doped semi-conducting layered materials, such as electron or hole doped MoS_2 or WS_2 [21] or electron doped PtX_2 (with X∈{S, Se, Te}) [58, 59] or InSe [60] could be suitable candidates due to reduced intra-band polarization (small effective electron/hole masses) as well as metallic 3*R*-NbS_2 and 1*T*-$AlCl_2$ due to their low internal plasmonic losses [44]. In contrast hole doped PtX_2 or InSe as well as conventional metallic 2H-phase TMDCs, such as TaS_2 or VS_2, are likely less preferable due their enhanced density of states (due to rather flat upmost valence bands) [58, 59, 61] and/or due to the close vicinity of the low-energy plasmon-hosting band to other fully occupied/empty bands which both increases the internal screening [44].

Additionally, layered materials with strongly anisotropic screening properties, such as doped black

phosphorus or T-phase WTe_2, have the potential to add another interesting degree of freedom to the proposed plasmonic waveguides: due to their strongly anisotropic plasmonic dispersions [49–52, 62] we expect the direction in which the plasmon dispersion is higher in energy to be more prone to the environmental screening due to the reduced effective mass in the corresponding direction. If this direction is parallel to the dielectric interfaces in the substrate the plasmonic confinement might be enhanced or achieved with reduced dielectric contrast. Otherwise, in case these two directions are perpendicular to each other the dielectric contrast in the environment might need to be strongly enhanced.

3.2. Structured environments

For the creation of structured environments, as needed for the proposed waveguides, we envision laterally grown and vertically cut materials, lithographic structures, twisted layered materials [63–65], or novel fractionalized 2D system [66–68] to be possible routes to pursue. As discussed above, the dielectric contrast in these structures should be rather high. Furthermore, it will be interesting to create environmental screening structures with more than just one or two dielectric interfaces. One could, for example, imagine periodically patterned substrates for optimal light–matter coupling, two-dimensional dielectric structures that either create plasmonic checkerboard patterns or plasmonic quantum dots, or non-linear plasmonic waveguides [69].

3.3. Conclusions

Our calculations suggest that it is feasible to externally functionalize a homogeneous 2D metallic layer by means of structured dielectric environments, thus creating new plasmonic waveguides using existing experimental techniques and available layered materials. In contrast to previous functionalization concepts, our approach only relies on a passive prestructured environment, to which the active layer needs to be exposed. Depending on the spatially modulated dielectric contrast in this environment plasmons can be confined within a 10 nm scale. At the same time, the described optimal excitation energy window for our proposal renders these devices highly specific to external stimuli allowing for switching or filtering applications. The optimization of these new plasmonic devices will thereby be a trade-off between the plasmonic localization and relative brightness which is controlled by the dielectric contrast in the heterogeneous environment.

Furthermore, we highlight that the described induced plasmonic functionality relies on spatial structuring of the dynamically screened Coulomb interaction within the material. Thus, it can also affect a variety of other many-body properties, including many-body excitations, such as magnons, and many-body instabilities, such as superconductivity or magnetism. The proposed plasmonic waveguide is therefore just one possible example of a more general concept for Coulomb-engineering of many-body properties in metallic layered materials with fascinating further applications.

Data availability statement

The data that support the findings of this study are available upon reasonable request from the authors.

Acknowledgments

The authors thank Frank Koppens, Mikhail I Katsnelson, and Henning Schlömer for useful discussions. This work was supported by the US Department of Energy under Grant Number DE-FG02-05ER46240. The numerical computations were carried out on the University of Southern California High Performance Supercomputer Cluster.

Appendix A. Background screening model

In vacuum the Coulomb interaction between two point charges q_1 and q_2 is simply given by $v(r) \propto q_1 q_2 / r$, where r is the distance between them. In the case of electrons within a realistic material the effective interaction between them is more complicated due to the polarizable environment [20, 21, 70]. In layered materials, this internal 'background' screening can be classically well approximated by a dielectric-slab model. As illustrated in figure 7, the electrons are supposed to be confined in the center ($z = 0$) plane of the dielectric slab, which is defined by the effective height h and the dielectric constant ε_m. These two parameters are determined from the intrinsic properties of the 2D material and can be calculated from first-principles [21, 36, 70]. Here we set $h = 5.76$ Å and $\varepsilon_\mathrm{m} = 10$ similar to the situation in transition mental dichalcogenide monolayers [37]. $\varepsilon_\mathrm{env1}$ and $\varepsilon_\mathrm{env2}$ are the environmental dielectric constants above and below the 2D material.

The 'background' screened Coulomb interaction $U(r)$ between two electrons in the $z = 0$ plane with a separation r can then be determined using an iterated image-charge ansatz [45, 71, 72]. The image charges (empty circles) generated by the real charge (solid circle) are shown in figure 7. In principle, there is an infinite number of image charges along the z-direction and their charges are determined by ε_m, $\varepsilon_\mathrm{env1}$, $\varepsilon_\mathrm{env2}$ and h. The full 'background' screened Coulomb interaction $U(r)$ on the $z = 0$ plane is given by the sum of all of these contributions. Here, we consider $\varepsilon_\mathrm{env1} = \varepsilon_\mathrm{env2} = \varepsilon_\mathrm{b}$. Then, $U(r)$ is given by

$$U(r) = \frac{e^2}{\varepsilon_\mathrm{m} r} + 2\sum_{n=1}^{\infty} \frac{e^2 \beta_\mathrm{b}^n}{\varepsilon_\mathrm{m} z_n(r)}, \qquad \text{(A1)}$$

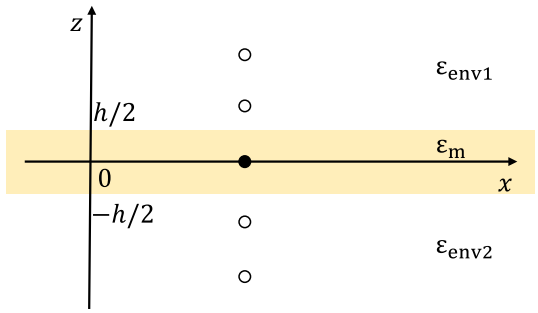

Figure 7. Internal screening in a 2D material along the $z=0$ plane modeled by a dielectric slab of height h with dielectric constant ε_m.

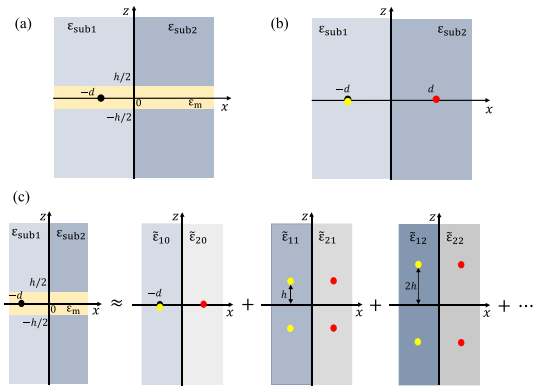

Figure 8. Image charge model of a 2D material embedded in a dielectric structure with a single vertical interface.

where $\beta_b = (\varepsilon_m - \varepsilon_b)/(\varepsilon_m + \varepsilon_b)$ and $z_n(r) = \sqrt{r^2 + (nh)^2}$. The first term in equation (A1) is the contribution from the real (source) charge, whereas the second term results from the image charges.

For the on-site interaction, i.e. $r=0$, the above formula diverges. To avoid this, we define the 'on-site' interaction at a slightly shifted position with a small separation δ above the source charge itself. In the numerical calculation we set $\delta = 0.85$ Å, which yields the on-site Coulomb energy to be 2.56 eV for the unsupported layer.

Appendix B. Image charge ansatz for spatially structured substrates

As soon as we additionally introduce vertical dielectric interfaces in the screening environment, the effective Coulomb interaction for $z=0$ can analytically only be approximately described. The configuration with a single vertical interface is illustrated in figure 8(a). In the following we put a real charge q (solid circle) on the $z=0$ plane at a distance of d to the vertical interface. The aim is to approximate the Coulomb potential on the full $z=0$ plane from this point charge.

To this end, we combine the analytically known solutions for the homogeneous dielectric slab (two parallel horizontal dielectric interfaces) with the homogeneous single dielectric interface situation depicted in figure 8(b). In the latter case the analytically correct potential can be constructed using a single additional image charge. In detail, if we place our source charge at $(-d, 0)$ (black dot in figure 8(b)) we will need an additional image charge at $(d, 0)$. For $\vec{r}_x < 0$ this yields

$$U(r) = \frac{e^2}{\varepsilon_{\text{sub}_1}} \left(\frac{1}{r_q} + \frac{\alpha_1}{r_1} \right) \tag{B1}$$

with $\alpha_1 = \frac{\varepsilon_{\text{sub}_1} - \varepsilon_{\text{sub}_2}}{\varepsilon_{\text{sub}_1} + \varepsilon_{\text{sub}_2}}$, $r_q = |\vec{r} + d\hat{x}|$ and $r_1 = |\vec{r} - d\hat{x}|$. For $\vec{r}_x > 0$ we correspondingly get

$$U(r) = \frac{e^2}{\varepsilon_{\text{sub}_2}} \left(\frac{1}{r_q} + \frac{\alpha_2}{r_2} \right) \tag{B2}$$

with $\alpha_2 = \frac{\varepsilon_{\text{sub}_2} - \varepsilon_{\text{sub}_1}}{\varepsilon_{\text{sub}_1} + \varepsilon_{\text{sub}_2}}$ and $r_2 = r_q$. This method is discussed in many text books and we refer the interested reader, e.g., to [71].

The Coulomb interaction on the $z=0$ plane, before introducing the vertical interface, is already discussed in appendix A and given by equation (A1), which we can slightly reformulate to

$$U(r) = \sum_{n=-\infty}^{\infty} \frac{e^2}{z_n(r)\tilde{\varepsilon}_{b,n}}. \tag{B3}$$

In this way, we can interpret $U(r)$ as the Coulomb interaction between an electron at r with a series of (electron) point charges positioned at z_n which are each embedded in different homogeneous dielectric backgrounds $\tilde{\varepsilon}_{b,n} = \varepsilon_m/\beta_b^{|n|}$.

Now, to model the effect of the additional vertical dielectric interface (between $\varepsilon_{\text{sub1}}$ and $\varepsilon_{\text{sub2}}$), we can introduce vertical image charges for each of these iterated horizontal image charge as described in equation (B1) and illustrated in figure 8. The full approximate interactions can thus be written as a summation of the form

$$U(r) = \sum_n U_n(r), \tag{B4}$$

where each $U_n(r)$ is evaluated as in the simple image charge method introduced before, however, with adjusted parameters. Specifically we need to replace $\varepsilon_{\text{sub}_1}$ and $\varepsilon_{\text{sub}_2}$ by $\tilde{\varepsilon}_{1,n}$ and $\tilde{\varepsilon}_{2,n}$ to evaluate $\alpha_{1,n}$ and $\alpha_{2,n}$, and replace r_q by $z_{n,q}(r) = \sqrt{r_q^2 + (nh)^2}$, r_1 by $z_{n,1}(r) = \sqrt{r_1^2 + (nh)^2}$ and r_2 by $z_{n,2}(r) = \sqrt{r_2^2 + (nh)^2}$. Altogether we get

$$U(r) = \begin{cases} \sum_n \frac{e^2}{\tilde{\varepsilon}_{1,n}} \left(\frac{1}{z_{n,q}(r)} + \frac{\alpha_{1,n}}{z_{n,1}(r)} \right), & \text{if } \vec{r}_x < 0, \\ \sum_n \frac{e^2}{\tilde{\varepsilon}_{2,n}} \left(\frac{2}{z_{n,q}(r)} + \frac{\alpha_{2,n}}{z_{n,2}(r)} \right), & \text{if } \vec{r}_x > 0. \end{cases} \tag{B5}$$

When two parallel vertical interfaces are introduced in the dielectric background, i.e. like the plasmonic waveguide configuration introduced in the

main text, we use the same concept. Now, however, we also need to introduce an infinite series of iterated image charges in x-direction.

Appendix C. Plasmonic excitations in real space

We aim to analyze the dielectric function

$$\varepsilon(\omega) = 1 - U\,\Pi_0(\omega) \tag{C1}$$

in real space. To this end we use the Coulomb interaction models from appendices A and B and evaluate the bare polarization Π_0 of the metallic band within the RPA. Since the the active metallic layer itself is translational invariant we can start in momentum space:

$$\Pi_0(\vec{q},\omega) = \frac{2}{\Omega_{\mathrm{BZ}}}\sum_{\vec{k}}\frac{f(\vec{k}) - f(\vec{k}+\vec{q})}{E(\vec{k}) - E(\vec{k}+\vec{q}) + \omega + i\gamma} \tag{C2}$$

with $E(\vec{k})$ being the non-interacting single-particle metallic-band dispersion at $\vec{k}$, $f(\vec{k})$ the corresponding Fermi function, and $\gamma = 0.02$ eV a finite broadening. The real-space representation in the atomic basis can then be obtained via an inverse Fourier transformation [73],

$$[\Pi_0(\omega)]_{ab} = \frac{1}{N}\sum_{\vec{q}}\Pi_0(q,\omega)e^{i\vec{q}\cdot(\vec{R}_a - \vec{R}_b)}. \tag{C3}$$

Here, the vectors $\vec{R}_{a/b}$ are defined on the real-space lattice. This two-step calculation greatly improves the computational efficiency. Finally, we obtain the real-space dielectric function as a matrix in the atomic basis via

$$[\varepsilon(\omega)]_{ab} = \delta_{ab} - \sum_{c} U(\vec{R}_a - \vec{R}_c)[\Pi_0(\omega)]_{cb}. \tag{C4}$$

The plasmonic excitations are identified from a spectral decomposition of this dielectric matrix,

$$\varepsilon(\omega) = \sum_{n}\varepsilon_n(\omega)|\phi_n(\omega)\rangle\langle\phi_n(\omega)|, \tag{C5}$$

by selecting the 'leading' dielectric eigenvalue $\varepsilon_{\max}(\omega)$ which maximizes the EELS $\mathrm{EELS}(\omega) \propto -\mathrm{Im}[1/\varepsilon_n(\omega)]$ together with its eigenvector $|\phi_{\max}(\omega)\rangle$ for each frequency. The real-space charge modulation of a plasmon mode at the frequency ω_p can be obtained from

$$|\rho_{\mathrm{ind}}(\omega_p)\rangle = \Pi_0(\omega_p)|\phi_{\mathrm{tot}}\rangle = \Pi_0(\omega_p)|\phi_{\max}(\omega_p)\rangle \tag{C6}$$

[74]. Here, we interpret the 'leading' eigenvector $|\phi_{\max}(\omega_p)\rangle$ as the total potential distribution at the plasmon frequency ω_p, since it solves the equation

$$\varepsilon(\omega)|\phi_{\mathrm{tot}}\rangle = |\phi_{\mathrm{ext}}\rangle \tag{C7}$$

when $|\phi_{\mathrm{ext}}\rangle = 0$, namely

$$\varepsilon(\omega_p)|\phi_{\max}(\omega_p)\rangle = 0\,|\phi_{\max}(\omega_p)\rangle, \tag{C8}$$

i.e. for $\varepsilon_{\max}(\omega_p) = 0$. The product $\Pi_0(\omega_p)|\phi_{\max}(\omega_p)\rangle$ then represents the induced charge distribution in the system. The full method has been reported in previous studies [66, 75, 76]. Finally, we note that by restricting the continuous position coordinates $\vec{r}$ and $\vec{r}'$ to the discretized lattice positions $\vec{R}_a$ and $\vec{R}_b$ we effectively neglect local-field effects [73].

ORCID iDs

Zhihao Jiang https://orcid.org/0000-0002-1170-2548
Malte Rösner https://orcid.org/0000-0002-6199-2176

References

[1] Hedin L 1965 New method for calculating the one-particle Green's function with application to the electron-gas problem *Phys. Rev.* **139** A796
[2] Aryasetiawan F and Gunnarsson O 1998 The GW method *Rep. Prog. Phys.* **61** 237
[3] Onida G, Reining L and Rubio A 2002 Electronic excitations: density-functional versus many-body Green's-function approaches *Rev. Mod. Phys.* **74** 601
[4] Kas J J, Rehr J J and Reining L 2014 Cumulant expansion of the retarded one-electron Green function *Phys. Rev.* B **90** 085112
[5] Steinhoff A, Florian M, Rösner M, Schönhoff G, Wehling T O and Jahnke F 2017 Exciton fission in monolayer transition metal dichalcogenide semiconductors *Nat. Commun.* **8** 1
[6] Barnes W L, Dereux A and Ebbesen T W 2003 Surface plasmon subwavelength optics *Nature* **424** 824
[7] Low T *et al* 2017 Polaritons in layered two-dimensional materials *Nat. Mater.* **16** 182
[8] Bill A, Morawitz H and Kresin Z 2003 Electronic collective modes and superconductivity in layered conductors *Phys. Rev.* B **68** 144519
[9] Hepting M *et al* 2018 Three-dimensional collective charge excitations in electron-doped copper oxide superconductors *Nature* **563** 374
[10] Van Wezel J, Schuster R, König A, Knupfer M, Van Den Brink J, Berger H and Büchner B 2011 Effect of charge order on the plasmon dispersion in transition-metal dichalcogenides *Phys. Rev. Lett.* **107** 176404
[11] Kogar A *et al* 2017 Signatures of exciton condensation in a transition metal dichalcogenide *Science* **358** 1314
[12] Oulton R F, Sorger V J, Genov D A, Pile D F and Zhang X 2008 A hybrid plasmonic waveguide for subwavelength confinement and long-range propagation *Nat. Photon.* **2** 496
[13] Ansell D, Radko I P, Han Z, Rodriguez F J, Bozhevolnyi S I and Grigorenko A N 2015 Hybrid graphene plasmonic waveguide modulators *Nat. Commun.* **6** 1
[14] Fang Y and Sun M 2015 Nanoplasmonic waveguides: towards applications in integrated nanophotonic circuits *Light: Sci. Appl.* **4** 294
[15] Ditlbacher H, Hohenau A, Wagner D, Kreibig U, Rogers M, Hofer F, Aussenegg F R and Krenn J R 2005 Silver nanowires as surface plasmon resonators *Phys. Rev. Lett.* **95** 257403
[16] Bozhevolnyi S I, Volkov V S, Devaux E, Laluet J Y and Ebbesen T W 2006 Channel plasmon subwavelength waveguide components including interferometers and ring resonators *Nature* **440** 508

[17] Schnell M, Alonso-González P, Arzubiaga L, Casanova F, Hueso L E, Chuvilin A and Hillenbrand R 2011 Nanofocusing of mid-infrared energy with tapered transmission lines *Nat. Photon.* **5** 283

[18] Boltasseva A, Volkov V S, Nielsen R B, Moreno E, Rodrigo S G and Bozhevolnyi S I 2008 Triangular metal wedges for subwavelength plasmon-polariton guiding at telecom wavelengths *Opt. Express* **16** 5252

[19] Kress S J *et al* 2015 Wedge waveguides and resonators for quantum plasmonics *Nano Lett.* **15** 6267

[20] da Jornada F H, Xian L, Rubio A and Louie S G 2020 Universal slow plasmons and giant field enhancement in atomically thin quasi-two-dimensional metals *Nat. Commun.* **11** 1

[21] Groenewald R E, Rösner M, Schönhoff G, Haas S and Wehling T O 2016 Valley plasmonics in transition metal dichalcogenides *Phys. Rev.* B **93** 205145

[22] Andersen K and Thygesen K S 2013 Plasmons in metallic monolayer and bilayer transition metal dichalcogenides *Phys. Rev.* B **88** 155128

[23] Liu Y, Willis R F, Emtsev K V and Seyller T 2008 Plasmon dispersion and damping in electrically isolated two-dimensional charge sheets *Phys. Rev.* B **78** 201403

[24] Gjerding M N, Pandey M and Thygesen K S 2017 Band structure engineered layered metals for low-loss plasmonics *Nat. Commun.* **8** 1

[25] Woessner A *et al* 2015 Highly confined low-loss plasmons in graphene-boron nitride heterostructures *Nat. Mater.* **14** 421

[26] Nikitin A Y, Guinea F, García-Vidal F J and Martín-Moreno L 2011 Edge and waveguide terahertz surface plasmon modes in graphene microribbons *Phys. Rev.* B **84** 161407

[27] Yuan S, Jin F, Roldán R, Jauho A P and Katsnelson M I 2013 Screening and collective modes in disordered graphene antidot lattices *Phys. Rev.* B **88** 195401

[28] Christensen J, Manjavacas A, Thongrattanasiri S, Koppens F H and García De Abajo F J 2012 Graphene plasmon waveguiding and hybridization in individual and paired nanoribbons *ACS Nano* **6** 431

[29] Kim J T and Choi S-Y 2011 Graphene-based plasmonic waveguides for photonic integrated circuits *Opt. Express* **19** 24557

[30] Thongrattanasiri S, Koppens F H and García De Abajo F J 2012 Complete optical absorption in periodically patterned graphene *Phys. Rev. Lett.* **108** 047401

[31] Vakil A and Engheta N 2011 Transformation optics using graphene *Science* **332** 1291

[32] Liu M, Yin X, Ulin-Avila E, Geng B, Zentgraf T, Ju L, Wang F and Zhang X 2011 A graphene-based broadband optical modulator *Nature* **474** 64

[33] Prishchenko D A, Mazurenko V G, Katsnelson M I and Rudenko A N 2018 Gate-tunable infrared plasmons in electron-doped single-layer antimony *Phys. Rev.* B **98** 201401

[34] Slotman G, Rudenko A, Van Veen E, Katsnelson M I, Roldán R and Yuan S 2018 Plasmon spectrum of single-layer antimonene *Phys. Rev.* B **98** 155411

[35] Iranzo D A *et al* 2018 Probing the ultimate plasmon confinement limits with a van der Waals heterostructure *Science* **360** 291

[36] Rösner M, Steinke C, Lorke M, Gies C, Jahnke F and Wehling T O 2016 Two-dimensional heterojunctions from nonlocal manipulations of the interactions *Nano Lett.* **16** 2322

[37] Steinke C, Wehling T O and Rösner M 2020 Coulomb-engineered heterojunctions and dynamical screening in transition metal dichalcogenide monolayers *Phys. Rev.* B **102** 115111

[38] Raja A *et al* 2017 Coulomb engineering of the bandgap and excitons in two-dimensional materials *Nat. Commun.* **8** 1

[39] Florian M, Hartmann M, Steinhoff A, Klein J, Holleitner A W, Finley J J, Wehling T O, Kaniber M and Gies C 2018 The dielectric impact of layer distances on exciton and trion binding energies in van der Waals heterostructures *Nano Lett.* **18** 2725

[40] Steinleitner P *et al* 2018 Dielectric engineering of electronic correlations in a van der Waals heterostructure *Nano Lett.* **18** 1402

[41] Utama M I B *et al* 2019 A dielectric-defined lateral heterojunction in a monolayer semiconductor *Nat. Electron.* **2** 60

[42] Kajino Y, Oto K and Yamada Y 2019 Modification of optical properties in monolayer WS2 on dielectric substrates by Coulomb engineering *J. Phys. Chem.* C **123** 14097

[43] van Loon E G C P, Schüler M, Springer D, Sangiovanni G, Tomczak J M and Wehling T O 2020 Coulomb engineering of two-dimensional Mott materials (arXiv:2001.01735)

[44] Andersen K, Latini S and Thygesen K S 2015 Dielectric genome of van der Waals heterostructures *Nano Lett.* **15** 4616

[45] Cho Y and Berkelbach T C 2018 Environmentally sensitive theory of electronic and optical transitions in atomically thin semiconductors *Phys. Rev.* B **97** 041409

[46] Lončarić I, Rukelj Z, Silkin V M and Despoja V 2018 Strong two-dimensional plasmon in Li-intercalated hexagonal boron-nitride film with low damping *npj 2D Mater. Appl.* **2** 33

[47] Lundeberg M B *et al* 2017 Tuning quantum nonlocal effects in graphene plasmonics *Science* **357** 187

[48] Low T and Avouris P 2014 Graphene plasmonics for terahertz to mid-infrared applications *ACS Nano* **8** 1086

[49] Low T, Roldán R, Wang H, Xia F, Avouris P, Moreno L M and Guinea F 2014 Plasmons and screening in monolayer and multilayer black phosphorus *Phys. Rev. Lett.* **113** 106802

[50] Prishchenko D A, Mazurenko V G, Katsnelson M I and Rudenko A N 2017 Coulomb interactions and screening effects in few-layer black phosphorus: a tight-binding consideration beyond the long-wavelength limit *2D Mater.* **4** 025064

[51] Wang C, Huang S, Xing Q, Xie Y, Song C, Wang F and Yan H 2020 Van der waals thin films of WTe_2 for natural hyperbolic plasmonic surfaces *Nat. Commun.* **11** 1158

[52] Wang C *et al* 2021 Tunable plasmons in large-area WTe_2 thin films *Phys. Rev. Appl.* **15** 014010

[53] Tame M S, McEnery K R, Özdemir ŠK, Lee J, Maier S A and Kim M S 2013 Quantum plasmonics *Nat. Phys.* **9** 329

[54] Jablan M, Buljan H and Soljačić M 2009 Plasmonics in graphene at infrared frequencies *Phys. Rev.* B **80** 245435

[55] Grigorenko A N, Polini M and Novoselov K S 2012 Graphene plasmonics *Nat. Photon.* **6** 749

[56] Luo X, Qiu T, Lu W and Ni Z 2013 Plasmons in graphene: recent progress and applications *Mater. Sci. Eng.* R **74** 351

[57] Kim M, Xu S G and Berdyugin A I *et al* 2020 Control of electron-electron interaction in graphene by proximity screenings *Nat. Commun.* **11** 2339

[58] Villaos R A B, Crisostomo C P, Huang Z-Q, Huang S-M, Padama A A B, Albao M A, Lin H and Chuang F-C 2019 Thickness dependent electronic properties of pt dichalcogenides *npj 2D Mater. Appl.* **3** 1

[59] Almayyali A O M, Kadhim B B and Jappor H R 2020 Tunable electronic and optical properties of 2dPtS2/MoS2 van der waals heterostructure *Physica* E **118** 113866

[60] Ding Y-m *et al* 2017 Enhancement of hole mobility inInSe monolayer via anInSe and black phosphorus heterostructure *Nanoscale* **9** 14682

[61] Lugovskoi A, Katsnelson M and Rudenko A 2019 Strong electron-phonon coupling and its influence on the transport and optical properties of hole-doped single-layer InSe *Phys. Rev. Lett.* **123** 176401

[62] Kiraly B *et al* 2019 Anisotropic two-dimensional screening at the surface of black phosphorus *Phys. Rev. Lett.* **123** 216403

[63] Bistritzer R and MacDonald A H 2011 Moiré bands in twisted double-layer graphene *Proc. Natl Acad. Sci. USA* **108** 12233

[64] Andrei E Y and MacDonald A H 2020 Graphene bilayers with a twist *Nat. Mater.* **19** 1265

[65] Weston A et al 2020 Atomic reconstruction in twisted bilayers of transition metal dichalcogenides *Nat. Nanotechnol.* **15** 592
[66] Westerhout T, Van Veen E, Katsnelson M I and Yuan S 2018 Plasmon confinement in fractal quantum systems *Phys. Rev.* B **97** 205434
[67] He T, Wang Z, Zhong F, Fang H, Wang P and Hu W 2019 Etching techniques in 2D materials *Adv. Mater. Technol.* **4** 1900064
[68] De Nicola F, Puthiya Purayil N S, Miŝeikis V, Spirito D, Tomadin A, Coletti C, Polini M, Krahne R and Pellegrini V 2020 Graphene plasmonic fractal metamaterials for broadband photodetectors *Sci. Rep.* **10** 6882
[69] Sahoo P K, Memaran S, Xin Y, Balicas L and Gutiérrez H R 2018 One-pot growth of two-dimensional lateral heterostructures via sequential edge-epitaxy *Nature* **553** 63
[70] Rösner M, Şaşlolu E, Friedrich C, Blügel S and Wehling T O 2015 Wannier function approach to realistic Coulomb interactions in layered materials and heterostructures *Phys. Rev.* B **92** 085102
[71] Jackson J D and Fox R F 1999 Classical electrodynamics *Am. J. Phys.* **67** 841
[72] Kumagai M and Takagahara T 1989 Excitonic and nonlinear-optical properties of dielectric quantum-well structures *Phys. Rev.* B **40** 12359
[73] Van Schilfgaarde M and Katsnelson M I 2011 First-principles theory of nonlocal screening in graphene *Phys. Rev.* B **83** 081409
[74] Fahimniya A, Lewandowski C and Levitov L 2020 Dipole-active collective excitations in moiré flat bands (arxiv:2011.02982)
[75] Wang W, Christensen T, Jauho A P, Thygesen K S, Wubs M and Mortensen N A 2015 Plasmonic eigenmodes in individual and bow-tie graphene nanotriangles *Sci. Rep.* **5** 9535
[76] Jiang Z, Rösner M, Groenewald R E and Haas S 2020 Localized plasmons in topological insulators *Phys. Rev.* B **101** 045106